JOURNAL OF PROPULSION AND POWER
Vol. 24, No. 6, November–December 2008

Flow Structure of Short-Length-Scale Disturbance in an Axial-Flow Compressor

Feng Lin*
Chinese Academy of Sciences, 100080 Beijing, People's Republic of China
Jingxuan Zhang†
Beijing University of Aeronautics and Astronautics, 100083 Beijing, People's Republic of China
and
Jingyi Chen*,‡ and Chaoqun Nie*
Chinese Academy of Sciences, 100080 Beijing, People's Republic of China

DOI: 10.2514/1.36525

Short-length-scale disturbances, also called *spikes*, are often responsible in triggering rotating stall in axial-flow compressors. One hypothesis suggests that spikes can be the consequence of dynamic interaction among forward-spilled tip-leakage flow, the main throughflow, and the reversed flow. However, the transit process of such a dynamic interaction in the vicinity of the rotor tip clearance and, thus, the physical images of the flow structure of a spike are still unknown. In this paper, we present a numerical study with a novel scheme for a low-speed axial-flow compressor by incorporating rotating inlet distortion. Because the inlet distortion will overload a portion of the blades while keeping the rest working normally, the short-length-scale disturbances can be observed without advocating the computational difficulty of simulating a fully stalled compressor. Two unsteady simulations using a commercial, three-dimensional, time-accurate, Reynolds-averaged Navier–Stokes solver are performed: one for a one-fourth rotor annulus with finer grids and the other for the entire rotor annulus with coarser grids. After the code is validated by comparing experimental results with the simulation for the entire rotor annulus, the one-fourth-annulus simulation is used to unveil the flow physics. As elucidated from the computational results, the complete birth-to-decay process of the short-length-scale disturbances is captured for the first time. The corresponding 3-D flow structure is also revealed. It is shown that the effects of dynamic flow interaction at the tip extend beyond the tip region and deeply into the blade span. A horn-shaped vortex with one end at about 30% of the blade span and the other end at the casing is formed, which generates a low-pressure dip in the casing-pressure measurement. The spike, as identified from casing-pressure measurement, corresponds to a flow image in which the vortex rotates around the annulus.

I. Introduction

ROTATING stall and surge are two instability modes of axial compression systems. Modern compressor designers increase aerodynamic loading on the blades dramatically to achieve lighter and shorter compressors. Rotating stall and surge limits such efforts, because heavy loading often results in flow instability. The system dynamics and the fluid dynamics of rotating stall are long-standing problems and continue to attract a great deal of attention.

The flow disturbances that appear before fully developed rotating stall play an important role in stall development and some of them are believed to trigger stall. The disturbances that actually trigger the system instability are called *stall precursors*. It is commonly recognized that *modes* and *spikes* are two basic types of stall precursors [1,2]. A number of studies have been carried out to understand the flow structure and dynamic response of modes and spikes [3–10]. Hoying et al. [4] presented multiblade unsteady numerical simulations of a compressor rotor and found that once the trace of tip-leakage vortex lined up with the leading edge of the blades, stall would follow. Vo et al. [6] summarized many computational efforts and presented two spike criteria that can be illustrated in Fig. 1 (from Fig. 11b of [6]). The leading-edge spillage of tip-leakage flow (due to the interface between tip-leakage flow and the main flow reaching the leading-edge plane) and the occurrence of reversed flow are hypothesized as two criteria of the emergence of spikes.

There are far fewer reports on experiments than on numerical simulations of spikes, mainly due to the technical difficulty in measuring the unsteady flows inside the blade passage in a rotating frame. Despite the advancements in technology such as particle image velocimetry and laser Doppler velocimetry, the most popular measurement method is still the casing-pressure measurement using pressure sensors. An early effort by Inoue et al. [7] obtained very interesting casing-pressure contours of both a short-length-scale stall cell and a long-length-scale stall cell. Inoue et al. then imagined that the short-length-scale stall cell might be a vortex similar to a tornado, with one end on the suction surface of the midspan of the blade and the other end on the casing. For later convenience, we copy the pressure contours and the artistic drawing of the vortex in Fig. 2. Inoue et al. explained their result with vortex theory and argued that the vortex obtained by Hoying et al. [4] should be of the same nature.

The results in Figs. 1 and 2a are plausible, yet the physical image of spikes as illustrated in Fig. 2b remains to be validated. The work of Vo et al. [6] did not go beyond the point of tip-leakage flow spillage, whereas the work of Inoue et al. [7] was a pure imagination based on reasoning from vortex theory. As a common practice, a spike is usually identified from the data trace of casing-pressure measurement. Figure 3 depicts a typical spike emerging on the time trace of measured casing-pressure data taken from our own experiments in previous research [11]. Three blade passages (or four blades) are involved, which are marked differently in Fig. 3. Closely observing the pressure pattern, one can easily notice an interesting, yet puzzling, phenomenon: the sawtooth profile is broken by a lower-pressure blade passage, a higher-pressure blade passage, and one in

Received 8 January 2008; revision received 29 June 2008; accepted for publication 21 July 2008.

*Professor, Institute of Engineering Thermophysics.
†Postdoctoral Researcher, School of Jet Propulsion.
‡Institute of Engineering Thermophysics; cjy@mail.etp.ac.cn (Corresponding Author).

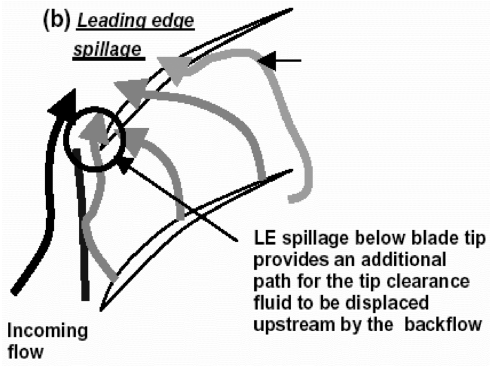

Fig. 1 Illustration of the spike criteria proposed by Vo et al. [6] (from Fig. 11b of [6]).

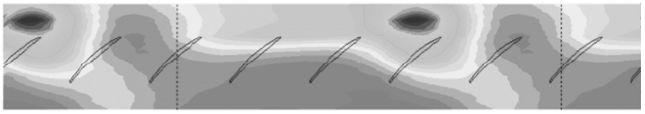

a)

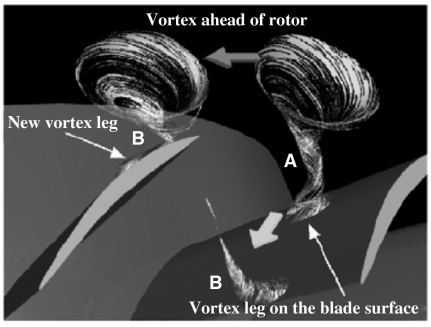

b)

Fig. 2 Casing-pressure contour and illustration of the tornadolike vortex by Inoue et al. [7] (from Figs. 5 and 6 of [7]).

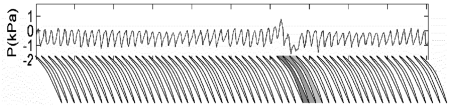

Fig. 3 A typical spike emerging on the time trace of measured casing-pressure data (from [11]).

the middle. Inoue et al.'s [7] data and many other measurements [2,12–16] exhibit the same pattern.

Although three may not be the magic number for the blade passages involved in a spike, what is repeatedly observed by many experimenters [12–16] is the fact that in a spike, a low-pressure region (which may cover multiple blade passages) is always accompanied by a high-pressure region, with a region of transition in the middle. If a vortex, such as that proposed by Inoue et al. [7], can be used to explain the low-pressure region, what happens in the high-pressure region? Why do they always appear in pairs? These questions cannot be answered without digging into the flow physics of the spike, which, in turn, will provide valuable insights for designing stall-free robust compressors.

The paper intends to answer the preceding questions by providing time-accurate flow images that reveal flow physics in detail. It will be organized as follows. In Section II, a novel idea is proposed to avoid the difficulty in numerical simulation of a stalled compressor, which was an obstacle preventing simulation of a spike because a spike is often followed immediately by a stall. The computational scheme is briefly explained in Sec. III, followed by the presentation of numerical results in Sec. IV. Discussions and conclusions will be presented in the last section.

II. Computational Approach

There are many computational efforts in simulating the stall-inception process in axial compressors [17–20], each of which possesses different approaches with their own research goals. For example, in the most recent work of Davis and Yao [20], a time-accurate single-blade-passage multiblade-row strategy is used to simulate the high-frequency unsteadiness due to self-excited flow at scales of the blade passage and rotor tip clearance as well as low-frequency unsteadiness due to longitudinal system modes. Because the purpose of the present paper is to explore the cross-passage flow dynamics in the tip region, a multiblade-passage configuration with enough details in the tip region has to be employed. Unsteady simulation that involves stalled flows is thus unavoidable. It is not unexpected that unsteady numerical simulation of a stalled compressor requires a great deal of computational resources. Chen and Hathaway [17] presented such an example, in which the simulations were run on an IBM P4 cluster at the Naval Oceanographic Office Major Shared Resource Center using 328 CPUs with 24 h (wall clock) computation time for one rotor revolution. There are 94 blade passages for the entire grid, with a total of 67 million grid points. The grid is partitioned into 328 blocks. With far less computational resources available to us, we have to seek alternative way to overcome the obstacle and achieve our goal.

The experimental results in [8] provide a clue to the solution. Inlet distortion, which is a topic of research interest on its own [21], can overload a portion of the rotor blades so much that this portion of blades starts to generate a short-length-scale disturbance (SLSD), whereas the rest of the blades still work quite normally. The overall performance of the compressor is still stable. The results in [8] also showed that SLSD could be eliminated in the clean (i.e., undistorted) sectors. These SLSDs are believed to be of the same nature as the spikes, because one of them eventually triggered rotating stall. Because we reserve the term *spike* for the special SLSD that actually triggers the stall, we will use the term SLSD for the rest of the paper, to infer the same phenomenon under study. The fact that the overall compressor performance is stable means that computation can be done in the same way as for a stable compressor, but this time we have the SLSD in our computational results. In other words, adding inlet distortion can help us avoid simulating a stalled compressor and still obtain valuable information about the flow physics of spikes. We chose counter-rotating inlet distortion for this computational study. There are two reasons for it:

1) For stationary inlet distortion, we learned from our own experiments (see [8]) that the same distortion screen at different locations might cause different stall-inception behavior (probably due to rotor whirl and asymmetric tip clearance). This makes the validation of our computational scheme nearly impossible.

2) For a corotating-inlet-distortion screen, the short-length-scale disturbances were generated much more frequently and violently because of the longer unsteady time scale observed by the blades.

The worst scenario happened when the propagation of the disturbances resonanced with the rotating speed of the distortion screen. We reported these experimental findings in [10].

III. Computational Scheme

The compressor selected for this investigation is actually the first rotor in a low-speed three-stage axial compressor, which was used in [10]. The blades are identical for the three stages. The size of tip clearance in the computation is consistent with that in the experiment rig. The design parameters are presented in Table 1.

Two types of distortion screens were simulated in the present paper. Screen 1×30 refers to one 30 deg screen, and screen 4×30 refers to four 30 deg screens placed symmetrically around the annulus. It should be noted that for screen 4×30, only one-fourth of the rotor blades are used, due to the symmetry of the geometry. Therefore, screen 4×30 allows more grids in the tip region, whereas the total number of grids is still fewer than screen 1×30 when the full rotor annulus is simulated. The total grid number of screens 4×30 and 1×30 is 2,027,805 and 3,718,757, respectively,

Table 1 Design parameters of the compressor

Parameter	Value
Rotational speed rpm	2400
Mass flow rate at the design point, kg/s	2.6
Outer diameter, mm	500
Hub-to-tip ratio	0.75
Rotor/stator axial gap, mm	8
Rotor blade number	58
Stator blade number	60
Rotor midspan stagger angle, deg	44
Stator midspan stagger angle, deg	23
Rotor tip clearance (% of tip chord)	2.4
Rotor/stator tip and midspan chord, mm	33.3

covering the entire computational domain that consists of the distortion screen and the rotor.

In the case of screen 4×30, there are 129 grids chordwise, 46 grids spanwise, and 20 grids pitchwise in each blade passage. Among them, there are 9 nodes within the tip gap. This adds up to 118,680 in each blade passage: a grid density comparable with many similar numerical simulations in the literature. In the case of screen 4×30, 15 blade passages are simulated. In the case of screen 1×30, 60 blade passages are included, and so grids in each blade passages are a little less than screen 4×30. We will use screen 4×30 to study the details of the flow structure in the tip region, and we will use screen 1×30 to observe large-scale behavior such as propagation of the spike around the annulus.

The validation of the computational scheme is made by comparing the results of screen 1×30 with in-house experiments (see the figures in the next section). Because the present research is qualitative in nature, the fact that the results of the case with few grids in each blade passage (screen 1×30) match with the experiments qualitatively guarantees that the case with more grids in each passage (screen 4×30) produces reliable qualitative results as well. For both cases, the distortion screen is placed inside the computational domain rather than treated as a boundary condition. Figure 4 depicts the computational geometry and grid distributions on the rotor blades and the hub.

A commercial solver package is used for the current study. The solver is a three-dimensional, viscous, time-accurate code employing an implicit second-order-accurate scheme to solve the unsteady Reynolds-averaged Navier–Stokes equations. The standard k-ε turbulence model and nonequilibrium wall functions are used to account for the turbulence flow. The same numerical solver was used in other research projects in past years and has been validated with experiments of an isolated rotor and a three-stage compressor with the same blades.

Steady boundary conditions were given at both the inlet and the outlet boundaries. The total pressure, total temperature, and inlet flow angle were specified uniformly at the inlet boundary, and the static-pressure distribution was specified at the outlet by means of a radial equilibrium law. Nonslip and adiabatic conditions were imposed all over the solid walls.

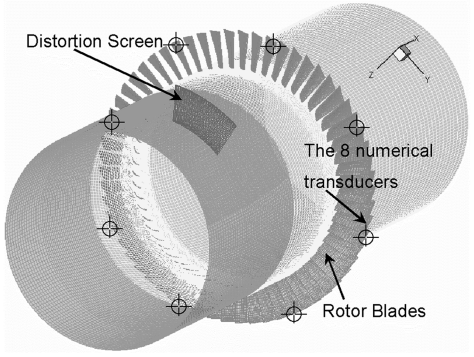

a) Screen 1x30

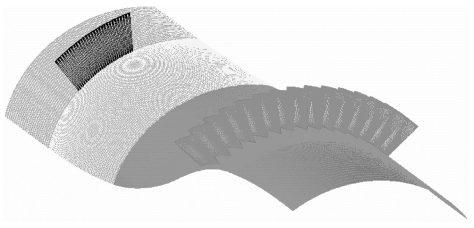

b) Screen 4x30

Fig. 4 Computational geometry and grid distributions on the blades, hub, and distortion screen for the a) 1×30 and b) 4×30 cases.

IV. Results

A. Code Validation

The results of computed rotor characteristics with screen 1×30 rotating in a direction opposite to rotor rotation with 20% of the rotor speed (herein noted as case $N02_{1\times30}$) is presented in Fig. 5. The experimental results are depicted in the same figure. One can see that they match each other well. Two operating points are labeled in the figure. The flows at point A are totally stable, whereas the SLSD has already been observed in the distorted sector at operating point B. Note that because the flowfield at point B is sufficient for the purposes of this paper, we stop our calculation at point B. However, it should be made clear that point B is not the calculated stall limit.

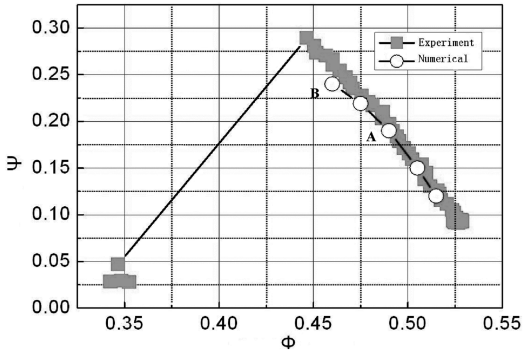

Fig. 5 Computed and experimental characteristics of the $N02_{1\times30}$ case of a single rotor.

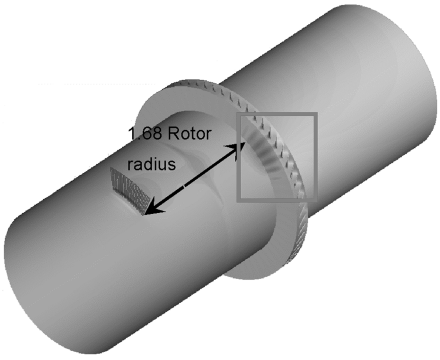

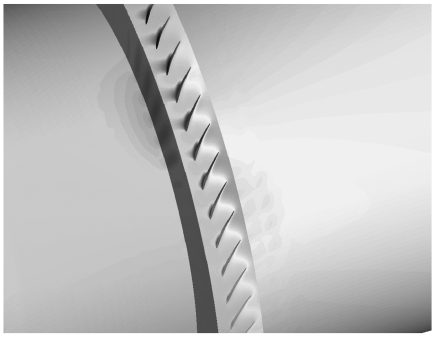

Fig. 6 Trace of the distorted region around the compressor annulus.

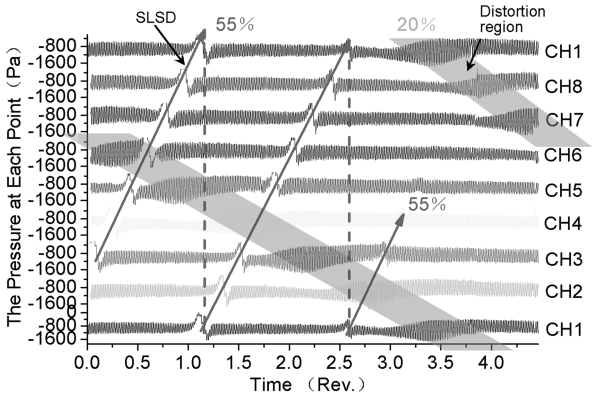

Fig. 7 Computed SLSD of case $N02_{1\times30}$.

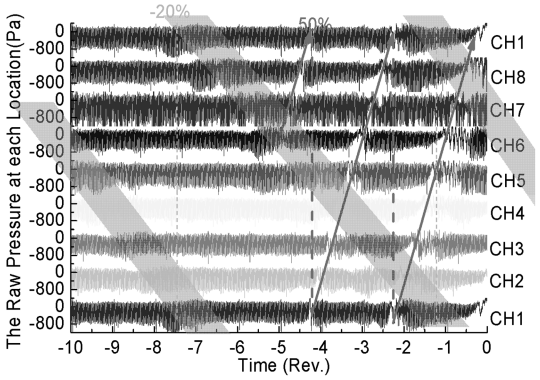

Fig. 8 Experimental SLSD of case $N02_{1\times30}$ (from Fig. 13 of [10]).

Figure 6 depicts the static-pressure contours of the whole compressor annulus, which shows how the distorted region spread in the compressor. The track of distorted flow forms a helix on the cylindrical surface of the compressor flow passage. When the distorted flow reaches the rotor blades, it reduces the axial velocity locally in the wake of the distortion screen and results in an increase of blade loading in the distorted sector.

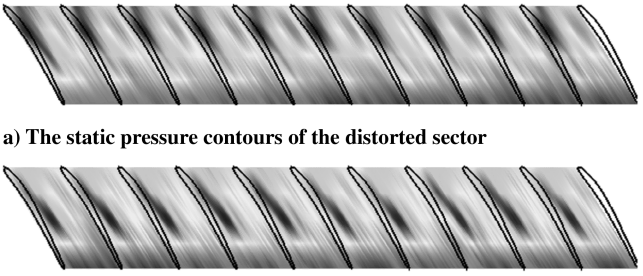

a) The static pressure contours of the distorted sector

b) The static pressure contours of the clean sector

Fig. 10 Experimental casing-pressure contours (from Fig. 4 of [10]).

Eight points around the rotor blades are chosen as the *numerical transducers*, in which the static pressure is recorded during the unsteady simulation (Fig. 4a). Figure 7 depicts a segment of the eight transducers' data in the $N02_{1\times30}$ case, in which a SLSD (labeled with an arrow) is clearly visible.

This result is then compared with the experimental results in Fig. 8 (from Fig. 13 of [10]). Both match with each other qualitatively well. Note that in Fig. 8, the disturbance is the spike because it triggers the stall. Thus, it is not surprising that the computed SLSD in Fig. 7 eventually decays, whereas the spike in Fig. 8 grows in time. We do this on purpose to demonstrate that other than the difference in growth and decay, the SLSD in Fig. 7 is qualitatively the same as the spike. Quantitatively, the propagation speed of the computed SLSD is 55% of the rotor speed, slightly higher than the experimental result (50% rotor speed).

Figure 9 depicts the computed casing-pressure contours for both distorted and clean sectors of case $N02_{1\times30}$. They are obtained at steady operating point A in Fig. 5. It can be observed that the aerodynamic loading center of the blades in the distorted sector is located much closer to the leading edge than that of the blades in the clean sector. This result can also be compared with the experimental result. Figure 10 (from Fig. 4 of [10]) shows the experimental casing-pressure contours for both distorted and clean sectors. It can be seen that the qualitative difference between the distorted sector (Fig. 10a)

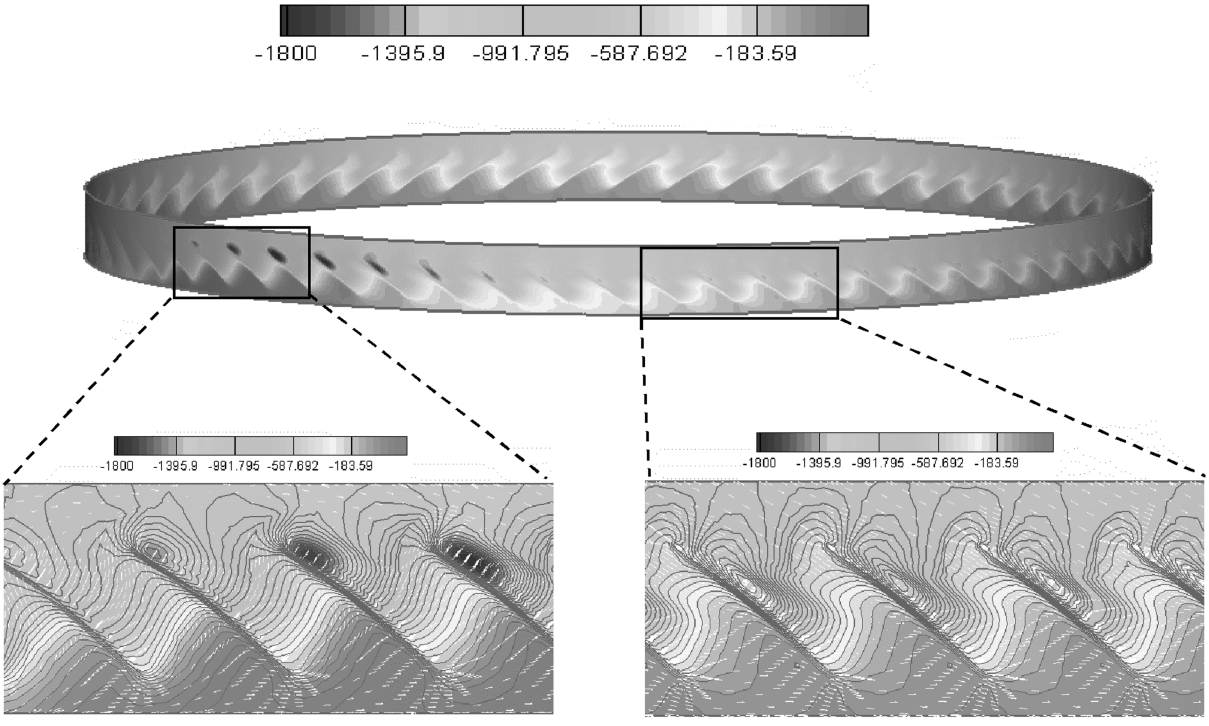

a) Distorted sector **b) Clean sector**

Fig. 9 Computed casing-pressure contours for both distorted and clean sectors of case $N02_{1\times30}$.

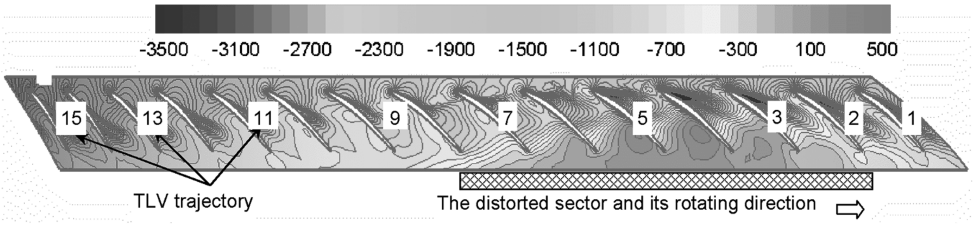

Fig. 11 Computed casing-pressure contours for case $N02_{4\times30}$.

and the clean sector (Fig. 10b) is captured in Figs. 9a and 9b, respectively. Given the fact the experimental contours were plotted based on the data from only five pressure probes along the chord, we are confident to state that the numerical simulation reproduces the experiments qualitatively well.

B. Unsteady-Flow Structure of a SLSD

To simulate the unsteady-flow structure of a SLSD, screen 4 × 30 rotating in a direction opposite to rotor rotation with 20% of the rotor speed (case $N02_{4\times30}$) is used. Figure 11 depicts an instant in which the rotor is operating stably with a large flow rate. One-fourth of the

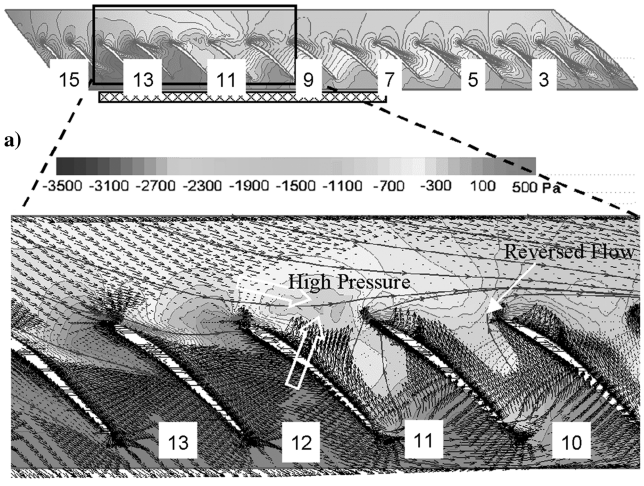

Fig. 12 Instantaneous pressure contours, velocity vectors, and streamlines at $\tau = 0$, the starting instant of a SLSD.

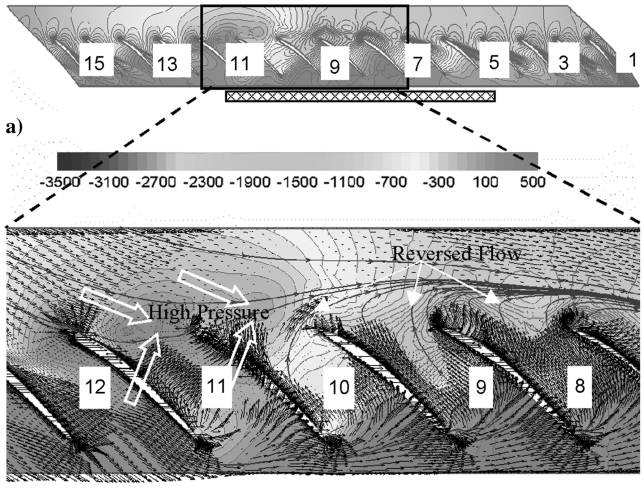

Fig. 13 Instantaneous pressure contours, velocity vectors, and streamlines at $\tau = 3T$.

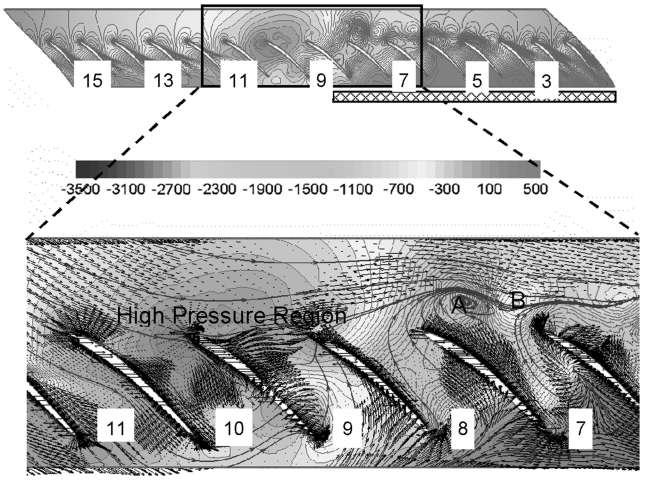

Fig. 14 Instantaneous pressure contours, velocity vectors, and streamlines at $\tau = 6T$.

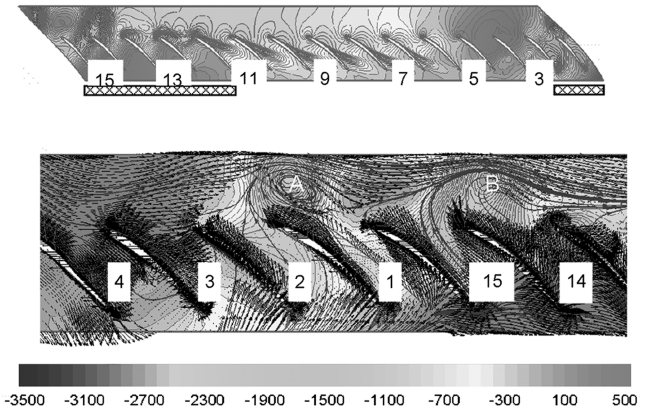

Fig. 15 Instantaneous pressure contours, velocity vectors, and streamlines at $\tau = 24T$.

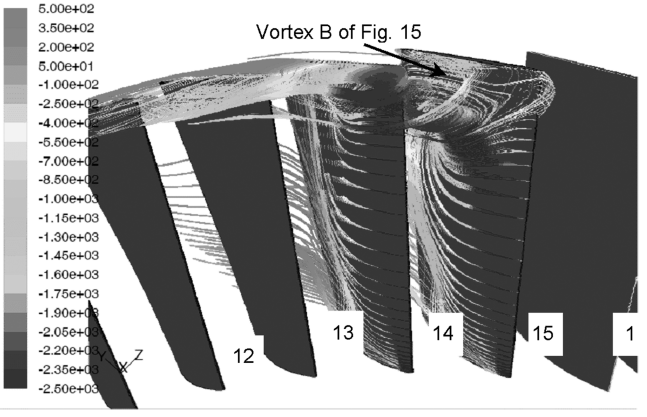

Fig. 16 Three-dimensional streamlines around vortex B in Fig. 15.

annulus is simulated, in which 15 blades are included in the computational domain. For convenience, we depict the flowfield in a relative frame that is fixed on the rotor. In this relative coordinate, the distorted sector rotates at a speed of 120% of the rotor speed relative to the rotor in a direction marked in Fig. 11. It can be seen that the distorted sector is a little wider (covering almost 6 blade passages in Fig. 11) than the distortion screen itself (covering almost 5 blade passages by design). Because the screen is located at a distance from the rotor so that when the low-energy region arrives at the rotor, it spreads wider than the screen itself. Similar to case $N02_{1\times30}$ (see Figs. 9 and 10), the distorted sector adds more aerodynamic loads to the blades. As a consequence, the tip-leakage vortices in these blade passages move forward, closer to the leading edge than those in the clean sector. Because this is an unsteady simulation, a time lag for the influence of the rotating distorted sector can be clearly seen. The first blade passage that just encounters the distorted sector is hardly influenced (passage 2), whereas the blade passage (passage 9) just out of the distorted sector is still under the influence of the distortion.

When the back pressure is high enough to overload the blades influenced by the distorted sector, the SLSD is born. Figures 12–14 present time-resolved flowfields of a SLSD at 3 subsequent time instants. The time intervals between these instants are marked with multiples of T, which is the time for one blade passage to sweep through a fixed point on casing: that is, one-sixtieth of the rotor period (as we have 60 blades in this simulated rotor). All of these figures together demonstrate the process of how a SLSD has taken its place from birth to growth. The time instant for Fig. 12 is at the starting moment of this process. Note that during the entire

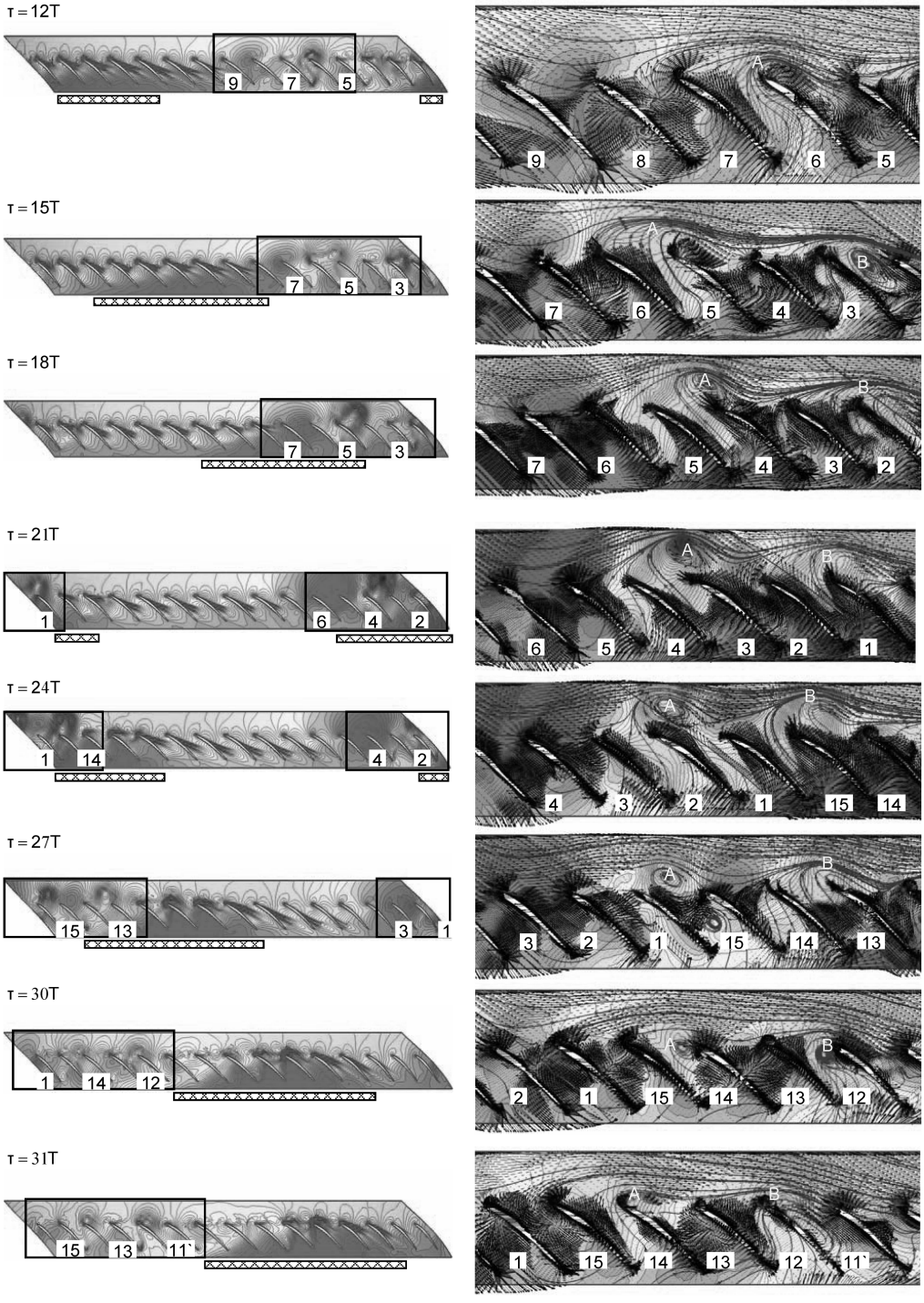

Fig. 17 Instantaneous pressure contours, velocity vectors, and streamlines for a sequence of time instants that demonstrate a complete life cycle of a short-length-scale disturbance.

simulation, the SLSD grows and decays cyclically as the distortion screen continues to circle around the compressor annulus. So the time moment for Fig. 12 is also the end of the previous life cycle of a SLSD.

On the relative coordinate fixed on the rotor, we label each blade passage from 1 to 15, as shown in Fig. 12a. Blade passages 10 to 13 are enlarged in Fig. 12b. Instantaneous velocity vectors (in black) and streamlines are also superimposed onto the same figure. The distorted sector can be recognized by checking the tip-leakage-vortex trajectories. The high-pressure zone covering blade passages 12 to 14 is actually a leftover from the last SLSD cycle. The blade loading and streamlines in this zone behave normally, even though the pressure in the entire zone is higher than the pressure outside. Blade passage 11 is of particular interest because the pressure difference across the blade between blade passages 11 and 12 (herein referred to as blades 11–12) is very high. The high-pressure difference causes strong tip-leakage flow, which impinges against the incoming main flow, creates a high-pressure region upstream (as marked directly on Fig. 12b), and deflects it away from this blade passage. This then creates a problem for blade passage 10, in which the axial pressure gradient is strongly negative. The deflected incoming main flow cannot bring enough axial momentum to overcome the negative pressure gradient, and thus a reverse flow in this blade passage is established. The same effect continues until blade passage 8, in which the incoming main flow finally returns into the blade passage again.

As time goes on, both the high-pressure region and the reversed-flow region will grow. Figure 13 is an example that depicts the flowfield at the instant $\tau = 3T$. The distorted sector moves about 3.5 blade passages during this time period. The strongest tip-leakage flow moves to blade passage 10, whereas the deflected main flow in blade passage 11 remains almost unchanged, due to the time lag of unsteady flows. As a consequence, the high-pressure region becomes stronger and expands to the front of blade passage 10. The reversed-flow region expands to blade passage 8.

This trend continues. The high-pressure region and the reversed-flow region both grow stronger and bigger while traveling along the rotating inlet distortion. At $\tau = 6T$, *the deflected main flow, the ever-strongest tip-leakage flow, and the reversed flow twist together and form a tornadolike vortex* that drifts away from the blade leading edge. Figure 14 depicts the scenario and shows that the high-pressure region is now covering blade passages 10 and 9; a vortex is clearly visible. Instantaneous streamlines show that it is consists of part of the main flow, the tip-leakage flow, and the reversed flow (labeled as A in black). Note that a portion of main flow that goes around this vortex impinges with the reversed flow and creates a new but smaller high-pressure region (labeled as *B* in black). This smaller high-pressure region then deflects the main flow again, which implies that a similar vortex-formation process may soon happen in a smaller scale.

Once the distorted sector leaves, vortex A and its associated high-pressure region will start to decay in the clean sector until another distorted sector approaches. To understand the 3-D structure of the vortex, 3-D streamlines at another time instant are depicted in Figs. 15 and 16. Figure 15 depicts the instantaneous pressure contours at $\tau = 24T$. Two vortices are observed. Vortices A and B and their associated high-pressure region are the SLSD, as observed from the casing-pressure measurement. Figure 16 depicts the 3-D flow structure of vortex B in Fig. 15 using instantaneous streamlines, on which the grayscale corresponds to values of static pressure along these lines. A vortex fairly similar to Inoue et al.'s [7] imagination (Fig. 2) is clearly seen. This vortex extends itself from the suction surface of blades 1–15 to the casing in the middle of blade passage 14 and involves streamlines from almost the entire blade span. This fact indicates that once this vortex is formed, the influence of the tip-clearance flow is no longer limited at the tip region. In Fig. 16, the vortex blocks nearly one-third of the blade span and has the potential to trigger a full stall.

Figure 17 depicts contours to demonstrate one typical process during which one distortion screen swept through the blades. It can be found that there are two vortices in all 15 rotor blade passages,

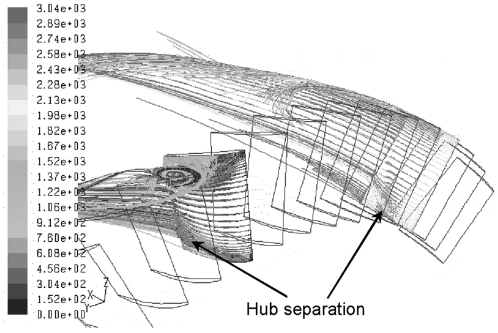

Fig. 18 Hub separation at the same instant as that of Fig. 16.

labeled with A and B at the low-pressure region (tornado vortex). Vortex A emerges earlier than the vortex B, and so at $\tau = 12T$ we only can see vortex A. The phenomenon that two vortices emerge successively is also found in the experimental results of [11]. The entire process of initiation, development, and decay of the vortices subjected to the interaction between main flow, leakage flow, and reversed flow is clearly recorded in Fig. 17. Such a process repeats many times as distortion screens rotate continuously, until one of them begins to grow adversely: at that moment, stall finally happens. For this reason, it is these vortices that are responsible for triggering the full stall.

V. Conclusions

The initiation and development process of a short-length-scale disturbance (SLSD) can be summarized as follows:

1) As the blades were overloaded, the high-pressure difference across the first highly loaded blade (blade 12–11 in Fig. 12) drove the tip-clearance flow upward and against the main flow, which created a high-pressure region just upstream of the leading edge and deflected the main incoming flow. The lack of incoming momentum due to the deflected main incoming flow caused the reversed flow in the equally loaded neighboring blade to be strong enough to spill out of the blade passage (blade passage 10 in Fig. 12). The chain reaction then took place in the next few blade passages until the main incoming flow reentered the rotor blades. This finding confirms the hypothesis of [6] on spike criteria. In fact, we captured the entire time-accurate process after leading-edge spillage of tip-clearance flow, the first of its kind in the open literature.

2) As time went on, the complex interaction of main flow, tip-leakage flow, and reversed flow became the key to the formation of short-length-scale disturbance. A 3-D vortex was formed, stretching from the blade's suction surface to the casing. This vortex looked like that described by Inoue et al. [7]. Its size was not limited in the vicinity of tip clearance, but was nearly one-third of the blade span.

3) The alternation of the high-pressure region (due to the impingement of tip-leakage flow and main flow) and the low-pressure region (due to the vortex) created the typical SLSD phenomenon, which can be observed from the casing-pressure signals (Fig. 3). Clear unsteady-flow structures for such a spike (which was originally defined based on the phenomenon found in casing-pressure signals) were obtained, tracked, and presented numerically (Fig. 17).

Experiment results [10,11] proved that this compressor exhibited spike stall inception. It is reasonable to believe that the stall in this compressor was initiated in the tip region, as we demonstrated in this paper that short-length-scale disturbances evolved from the tip region and extend into one-third of the blade span. At the same time, one can see that there was a separation in the hub region of the blade, as shown in Fig. 16. We further noticed that this kind of hub separation existed on other blades' suction surfaces too, regardless of whether there was a SLSD in the tip region of that blade or not (Fig. 18), and it did not rotate within the annulus relative to the rotor. Therefore, we conclude that this separation did not cause the stall.

The research of this paper was done on a low-speed compressor. The flow structure of spikes in a high-speed compressor is still under

investigation. Nevertheless, the authors are confident that the results in a low-speed compressor will surely provide guidance and reference for the high-speed-compressor research.

The role of tip-leakage flow in a spike initiation, as demonstrated in this paper, can also help in designing an effective stall controller with minimum costs in efficiency and device complexity. The successful demonstration of microinjection [22] sheds light in this direction.

Acknowledgments

This research is supported by the National Science Foundation of China through grants 50736007 and 50676094. Feng Lin is also supported by the Chinese Academy of Sciences through the 100-Scholar Project. The support is gratefully acknowledged.

References

[1] Garnier, V. H., Epstein, A. H., and Greitzer, E. M., "Rotating Waves as a Stall Inception Indication in Axial Compressors," *Journal of Turbomachinery*, Vol. 113, Apr. 1991, pp. 290–302. doi:10.1115/1.2929105

[2] Day, I. J., "Stall Inception in Axial Flow Compressors," *Journal of Turbomachinery*, Vol. 115, Jan. 1993, pp. 1–9. doi:10.1115/1.2929209

[3] Camp, T. R., and Day, I. J., "A Study of Spike and Modal Stall Phenomena in a Low-Speed Axial Compressor," *Journal of Turbomachinery*, Vol. 120, July 1998, pp. 393–401.

[4] Hoying, D. A., Tan, C. S., Vo, H. D., and Greitzer, E. M., "Role of Blade Passage Flow Structures in Axial Compressor Rotating Stall Inception," *Journal of Turbomachinery*, Vol. 121, Oct. 1999, pp. 735–742.

[5] Davis, R. L., and Yao, J., "Prediction of Compressor Stage Performance from Choke through Stall," *Journal of Propulsion and Power*, Vol. 22, No. 3, 2006, pp. 550–557. doi:10.2514/1.15463

[6] Vo, H. D., Tan, C. S., and Greitzer, E. M., "Criteria for Spike Initiated Rotating Stall," American Society of Mechanical Engineers Paper GT2005-68374, June 2005.

[7] Inoue, M., Kuroumaru, M., Tanino, T., Yoshida, S., and Furukawa, M., "Comparative Studies on Short and Long Length-Scale Stall Cell Propagating in an Axial Compressor Rotor," American Society of Mechanical Engineers Paper GT2000-0425, May 2000.

[8] Lin, F., Li, M. L., and Chen, J. Y., "Long-to-Short Length Scale Transition: a Stall Inception Phenomenon in an Axial Compressor with Inlet Distortion," *Journal of Turbomachinery*, Vol. 128, Jan. 2006, pp. 130–140. doi:10.1115/1.2098808

[9] Lin, F., Li, M. L., and Chen, J. Y., "Wavelet Analysis of Rotor-Tip Disturbances in Axial-Flow Compressor," *Journal of Propulsion and Power*, Vol. 20, 2, 2004, pp. 319–334. doi:10.2514/1.9257

[10] Zhang, J. X., Lin, F., Chen, J. Y., and Nie, C. Q., "The Flow Mechanism of How Distorted Flows Deteriorate Stability of an Axial Compressor," American Society of Mechanical Engineers Paper GT2007-27268, May 2007.

[11] Zhang, J. X., "The Unsteady Mechanism and the Role of Tip Clearance Flow in Distortion Induced Instability in an Axial Compressor," Ph.D. Dissertation, Inst. of Engineering Thermophysics, Chinese Academy of Sciences, Beijing, 2007.

[12] Day, I. J., and Freeman, C., "The Unstable Behavior of Low and High Speed Compressors," *Journal of Turbomachinery*, Vol. 116, Apr. 1994, pp. 194–201. doi:10.1115/1.2928353

[13] Dobat, A., Saathoff, H., and Wulff, D., "Experimentelle Untersuchungen zur Entstehung von Rotating Stall in Axialventilatoren," *VDI-Berichte*, Vol. 1591, Feb. 2001, pp. 345–360.

[14] Silkowski, P. D., "Measurements of Rotor Stalling in a Matched and Mismatched Multistage Compressor," Gas Turbine Lab., Massachusetts Inst. of Technology Rept. 221, Cambridge, MA, 1995.

[15] Tahara, N., Kurosaki, M., Ohta, Y., Outa, E., Nakakita. T., and Tsurumi, Y., "Early Stall Warning Technique for Axial Flow Compressors," American Society of Mechanical Engineers Paper GT2004-53292, June 2004.

[16] Park, H. G., "Unsteady Disturbance Structures in Axial Flow Compressor Stall Inception," M.S. Thesis, Massachusetts Inst. of Technology, Cambridge, MA, 1994.

[17] Chen, J. P., and Hathaway, M. D., "Pre-Stall Behavior of a Transonic Axial Compressor Stage via Time-Accurate Numerical Simulation," American Society of Mechanical Engineers Paper GT2007-27926, May 2007.

[18] He, L., "Computational Study of Rotating-Stall Inception in Axial Compressors," *Journal of Propulsion and Power*, Vol. 13, 1, 1997, pp. 31–38. doi:10.2514/2.5147

[19] Saxer-Felici, H. M., Saxer, A. P., Inderbitzin, A., and Gyarmathy, G., "Numerical and Experimental Study of Rotating Stall in an Axial Compressor Stage," *AIAA Journal*, Vol. 38, 7, 2000, pp. 1132–1141. doi:10.2514/2.1106

[20] Davis, R. L., and Yao, J., "Computational Approach for Predicting Stall Inception in Multistage Axial Compressors," *Journal of Propulsion and Power*, Vol. 23, 2, Mar.–Apr., 2007, pp. 257–265. doi:10.2514/1.18442

[21] Lin, F., and Chen, J. Y., "Theoretical Study of Inlet-Distortion-Induced Instability of Axial Compression Systems," *Proceedings of the Institution of Mechanical Engineers Part A, Journal of Power Engineering*, Vol. 220, No. 4, 2006, pp. 327–342. doi:10.1243/09576509A07704

[22] Nie, C. Q., Xu, G., Cheng, X. B., and Chen, J. Y., "Micro Tip Injection and Its Unsteady Response in a Low-Speed Axial Compressor," *Journal of Turbomachinery*, Vol. 124, No. 4, 2002, pp. 572–579. doi:10.1115/1.1508383

A. Prasad
Associate Editor